International Journal of Multiphase Flow 179 (2024) 104924

Contents lists available at ScienceDirect

International Journal of Multiphase Flow

journal homepage: www.elsevier.com/locate/ijmulflow

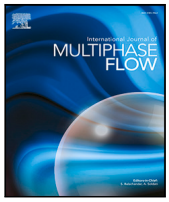

Vapor bubble nucleation in flowing liquids

M. Gallo *, C.M. Casciola

Department of Mechanical and Aerospace Engineering, Sapienza University of Rome, via Eudossiana 18, 00184 Rome, Italy

ARTICLE INFO

Keywords:
Cavitation
Boiling
Diffuse interface
Phase change
Fluctuating hydrodynamics

ABSTRACT

In this work, a stochastic diffuse interface model coupled with the Navier–Stokes equations has been exploited to numerically investigate vapor nucleation in a non-equilibrium system (a flowing liquid). Both homogeneous and heterogeneous nucleation is addressed and the influence of macroscopic flows on nucleation observables is discussed. The extended mesoscale simulations allow us to infer the spatial distributions of the nucleated bubbles via Voronoi tessellation analysis and to represent the nucleation phenomenon as a stochastic Random Poisson Point process. The findings open the way to design multiscale fluid simulations experiencing phase change.

1. Introduction

First-order phase transitions show similarities across a wide spectrum of physical contexts, such as bubble/drop nucleation in metastable fluids (Debenedetti, 1996), crystallization (Lutsko, 2019), or vesicle fusion/fission (Steinkühler et al., 2020; Bottacchiari et al., 2022, 2024). Nucleation originates at the atomistic scale where critical nuclei appear due to the rare thermal fluctuation (a rare event) able to overcome the free energy barrier. The phenomenology successively develops on macroscopic scales after the growth of the nucleated phase. Here we focus on the liquid–vapor phase transition (i.e. cavitation, induced by pressure decrease, or boiling, due to temperature increase) when the nucleation process and the bubble dynamics are coupled to macroscopic hydrodynamics. To this purpose, a stochastic diffuse interface model is exploited to address the cavitation dynamics in macroscopic flows bounded by solid walls.

Cavitation is the main cause of damage (Tomita and Shima, 1986; Abbondanza et al., 2022, 2023) to ship propellers, engine injectors, spillways in dams (Tomita and Shima, 1986; Abbondanza et al., 2022) and it is exploited in many chemical reactors and cleaning systems (Ohl et al., 2006). Vapor bubble formation near solid hot surfaces is an efficient cooling process due to the latent heat of evaporation, and as such is an extremely active research field (Zhang et al., 2022, 2023; Gallo et al., 2023; Chakraborty et al., 2024; Municchi et al., 2024). Ultrasound-induced cavitation is currently employed in medicine (Brennen, 2015) for tumour treatment and surgical application (Miller and Song, 2003; Brentnall et al., 2001). It is also used to enhance biological barrier permeability for drug and gene delivery (Silvani et al., 2019).

Nucleation is classically described in terms of a single bubble appearing in the metastable, bulk liquid (homogeneous nucleation). The free-energy profile – a function of bubble size/radius – attains a maximum in correspondence with the critical size. Central objects of the theory are nucleation rates (number of bubbles formed per unit time and volume), critical nuclei, and free energy barriers (free energy difference between critical value and pure liquid).

The thermodynamic parameters affecting nucleation are the reduced density of the metastable liquid ρ, and, in the presence of solid walls, the equilibrium Young contact angle ϕ, accounting for the wall wettability ($\phi \lessgtr 90°$ for hydrophilic and hydrophobic walls, respectively). In a flowing liquid, two additional parameters need to be considered. One is the Reynolds number, $\mathrm{Re} = \rho\dot{\gamma}L^2/\mu$, where $\dot{\gamma}$ is the typical shear rate, and L is the flow length scale (e.g., the width of the channel through which the liquid is flowing), with μ the fluid viscosity. The other one is the capillary number $\mathrm{Ca} = \mu\dot{\gamma}\ell/\sigma$, where σ is the surface tension and ℓ is the length scale relevant to the capillary phenomena. For nucleation, ℓ is conveniently identified with the diameter of the critical nucleus D^*. Depending on the specific context, the Reynolds numbers can range from small values in micro/nanofluidics to extremely large ones, like, e.g, in hydraulic applications. To the opposite, the capillary number is typically small, given the nanometer-sized critical nucleus and the limited shear rate. In extreme cases however, $\dot{\gamma}$ can be as large as $1. \times 10^8\,\mathrm{s}^{-1}$, like in the bearings of turbochargers and cryogenic turbo pumps running at $30 \div 250 \times 10^3$ rpm with liquid lubrication films on the order of $1 \div 100\,\mu\mathrm{m}$ and velocity differences across the lubricating layer on the order of $60\,\mathrm{m/s}$ (Qiu et al., 2017). In these conditions a reasonable range for the capillary number can be $\mathrm{Ca} \in \left[0 \div 10^{-1}\right]$. To focus the attention on the near wall region while allowing for the numerical simulation of the nucleating flow, the relevant Reynolds number range is here limited to $\mathrm{Re} \leq 300$.

* Corresponding author.
E-mail addresses: mirko.gallo@uniroma1.it (M. Gallo), carlomassimo.casciola@uniroma1.it (C.M. Casciola).

https://doi.org/10.1016/j.ijmultiphaseflow.2024.104924
Received 15 March 2024; Received in revised form 6 June 2024; Accepted 18 July 2024
Available online 23 July 2024

As pointed out in Menzl et al. (2016), Gallo et al. (2020) and Magaletti et al. (2021), the classical nucleation theory (CNT) fails because it ignores microscopic information such as curvature dependence of surface tension and thermal fluctuations. These ingredients are naturally present in microscopic approaches based on molecular dynamics (MD) (Chen et al., 2001, 2005; Kathmann et al., 2009; Diemand et al., 2013) and dynamic density functional theory (DDFT) (Goddard et al., 2012; Lutsko, 2012; Durán-Olivencia et al., 2017; Lutsko, 2019). These approaches are however limited to small spatial and temporal scales, preventing the full-fledged study of bubble evolution from nucleation to fully non-linear bubble dynamics. It is well known that the activation barrier is amazingly reduced by impurities suspended in the liquid or by bounding solid walls (heterogeneous nucleation (Blander and Katz, 1975)) where the process is influenced by the geometry and the wettability of the solid.

If much is still to be understood about the bubble formation process in a quiescent environment, even less is known concerning the coupling with hydrodynamic motion. In engineering, the problem is dealt with macroscopic formulations (Zhang et al., 2018; Maeda et al., 2018) where the spatial distribution of bubble nuclei are assumed *a priori* in a sort of one-way coupling approach between pre-existing nuclei and fluid flow. Vapor embryos are localized density depletion regions in the liquid where low-pressure zones are encountered. This typically happens at solid surfaces which, depending on wall wettability and smoothness, are preferential sites for nucleation. Bubbles survive and grow as long as they are confined in low-pressure regions to suddenly become unstable and collapse at higher pressures. Interestingly the macroscopic flows also influence the microscopic physics of the nucleation, where out-of-equilibrium thermodynamic systems show different nucleation rates at the same thermodynamic metastability (Heymann and Vanden-Eijnden, 2008). These shreds of evidence shed light on the interconnection of different spatial scales involved in the thermally activated process in non-equilibrium conditions.

Despite the fundamental and technological relevance of flow-induced nucleation, liquid–vapor phase change in hydrodynamic flows has never been addressed so far due to the intrinsic difficulty of coupling the nucleation process and hydrodynamic fields. In this work we address (i) the effect of hydrodynamics on the nucleation rate; (ii) the spatial distribution of the nucleation embryos; and (iii) the respective role of heterogeneous and homogeneous nucleation.

2. Mathematical model

The effect of solid walls on nucleation is confined to a narrow layer near the boundary where the shear stress is the largest. The prototypal problem is a liquid layer nucleating bubbles while flowing over a flat smooth wall, like in a Couette flow. This is the flow configuration we address by exploiting a model that consists of a set of stochastic partial differential equations for the mass, momentum, and energy densities

$$\begin{aligned}
\frac{\partial \rho}{\partial t} + \boldsymbol{\nabla}\cdot(\rho\mathbf{u}) &= 0, \\
\frac{\partial \rho\mathbf{u}}{\partial t} + \boldsymbol{\nabla}\cdot(\rho\mathbf{u}\otimes\mathbf{u}) &= \boldsymbol{\nabla}\cdot\boldsymbol{\Sigma} + \boldsymbol{\nabla}\cdot\boldsymbol{\delta\Sigma}, \\
\frac{\partial E}{\partial t} + \boldsymbol{\nabla}\cdot(\mathbf{u}E) &= \boldsymbol{\nabla}\cdot(\mathbf{u}\cdot\boldsymbol{\Sigma}-\mathbf{q}) + \boldsymbol{\nabla}\cdot(\mathbf{u}\cdot\boldsymbol{\delta\Sigma}-\boldsymbol{\delta q}),
\end{aligned} \tag{1}$$

where $\rho(\mathbf{x},t)$ is the fluid density, $\mathbf{u}(\mathbf{x},t)$ is the fluid velocity, $E(\mathbf{x},t)$ is the total energy density, $E = \mathcal{U}_b + 1/2\rho|\mathbf{u}|^2 + 1/2\lambda|\boldsymbol{\nabla}\rho|^2$, with $\mathcal{U}_b$ the bulk internal energy density. The deterministic part of the model (Kortweg–Navier–Stokes equations) accounts for the stress tensor and the energy flux.

$$\begin{aligned}
\boldsymbol{\Sigma} &= \left[-p + \frac{\lambda}{2}|\boldsymbol{\nabla}\rho|^2 + \rho\boldsymbol{\nabla}\cdot(\lambda\boldsymbol{\nabla}\rho)\right]\boldsymbol{I} - \lambda\boldsymbol{\nabla}\rho\otimes\boldsymbol{\nabla}\rho + \mu\left[(\boldsymbol{\nabla}\mathbf{u}+\boldsymbol{\nabla}\mathbf{u}^T) - \frac{2}{3}\boldsymbol{\nabla}\cdot\mathbf{u}\boldsymbol{I}\right], \\
\boldsymbol{q} &= \lambda\rho\boldsymbol{\nabla}\rho\boldsymbol{\nabla}\cdot\mathbf{u} - k\boldsymbol{\nabla}\theta.
\end{aligned}$$

Where $p(\mathbf{x},t)$ the thermodynamic pressure, λ is the capillary coefficient, and $\theta(\boldsymbol{x},t)$ the temperature field (Magaletti et al., 2016). They include two contributions, the dissipative component depending on viscosity μ and thermal conductivity k, and the reversible contribution. The latter comes from the square-gradient free energy,

$$F = \int_V \left[f_b(\theta,\rho) + \frac{\lambda}{2}|\nabla\rho|^2\right]dV + \int_A f_w(\theta,\rho)dS$$

(e.g. $\nabla\cdot\boldsymbol{\Sigma}_{rev} = -\rho\nabla\delta F/\delta\rho + \theta\nabla\delta F/\delta\theta$), where f_b is the free energy density of the homogeneous fluid. f_w accounts for the fluid–solid interaction (i.e. for the solid wettability), and determines the boundary condition for the mass density, $\lambda\partial\rho/\partial n|_{\partial V} = df_w/d\rho(\rho,\theta)$. The wall free energy is obtained from the Young contact angle ϕ and the bulk fluid free energy such that $df_w/d\rho = \cos\phi\sqrt{2\lambda\left(\omega_b(\rho,\theta)-\omega_b\left(\rho_V\right)\right)}$, where $\omega_b = f_b - \rho\partial f_b/\partial\rho$ (Gallo et al., 2021). The noise terms in the momentum and energy equations ($\delta\boldsymbol{\Sigma}$ and $\delta\mathbf{q}$) induce fluctuations tailored to reproduce the equilibrium Einstein–Boltzmann probability distribution in the spirit of Landau–Lifshitz fluctuating hydrodynamics. They are delta-correlated Gaussian processes with covariance dictated by the Fluctuation Dissipation Balance (FDB) (Chaudhri et al., 2014; Gallo et al., 2021).

$$\begin{aligned}
\langle\boldsymbol{\delta\Sigma}(\hat{x},\hat{t})\otimes\boldsymbol{\delta\Sigma}^{\dagger}(\tilde{x},\tilde{t})\rangle &= \mathbf{Q}^{\boldsymbol{\Sigma}}\delta(\hat{x}-\tilde{x})\delta(\hat{t}-\tilde{t}), \\
\langle\boldsymbol{\delta q}(\hat{x},\hat{t})\otimes\boldsymbol{\delta q}^{\dagger}(\tilde{x},\tilde{t})\rangle &= \mathbf{Q}^{\mathbf{q}}\delta(\hat{x}-\tilde{x})\delta(\hat{t}-\tilde{t}),
\end{aligned} \tag{2}$$

where

$$\begin{aligned}
\mathbf{Q}^{\boldsymbol{\Sigma}}{}_{\alpha\beta\nu\eta} &= 2\mathrm{k}_B\theta\mu(\delta_{\alpha\nu}\delta_{\beta\eta} + \delta_{\alpha\eta}\delta_{\beta\nu} - \frac{2}{3}\delta_{\alpha\beta}\delta_{\nu\eta}), \\
\mathbf{Q}^{\mathbf{q}}_{\alpha\beta} &= 2\mathrm{k}_B\theta^2 k\delta_{\alpha\beta}.
\end{aligned} \tag{3}$$

A final ingredient is the equation of state for the bulk fluid, a Lennard-Jones (LJ) fluid, in this case, Johnson et al. (1993), see Gallo et al. (2018b) for comparison with molecular dynamics.

3. Numerical setup

The flow we aim to address consists of a stochastic Couette Flow, where the motion is driven by the upper wall $\mathbf{u}(x,y,L)\cdot\hat{\mathbf{x}} = U_{wall}$. Periodicity in the streamwise (x) and spanwise (y) directions is assumed. The system volume is $V = 500\times500\times2000$, discretized with $50\times50\times200$ points on an equispaced grid. The simulation setup is summarized in Fig. 1. All quantities are made dimensionless with the following reference quantities: $L_{ref} = \sigma = 3.4\times10^{-10}$ m as length, $E_{ref} = \epsilon = 1.65\times10^{-21}$ J as energy, $\theta_{ref} = \epsilon/k_B$ as temperature, $m = 6.63\times10^{-26}$ Kg as mass, $U_{ref} = \sqrt{\epsilon/m}$ as velocity, $T_{ref} = L_{ref}/U_{ref}$ as time. To determine the grid spacing we performed preliminary grid sensitivity tests on the nucleation rate (the most relevant observable in nucleation processes).

The equations are numerically solved with the method of lines using staggered central finite differences for spatial discretization (Balboa

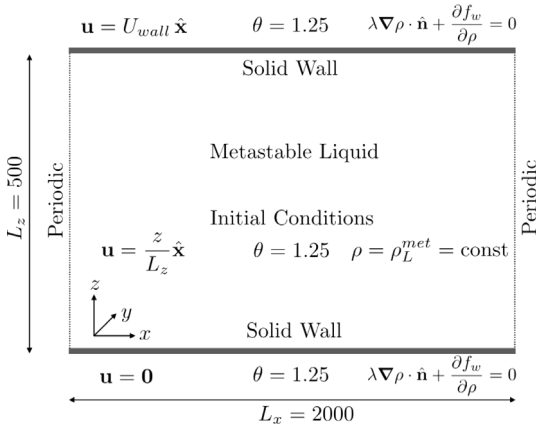

Fig. 1. Top panel: Simulation setup sketch for the stochastic Couette Flow.

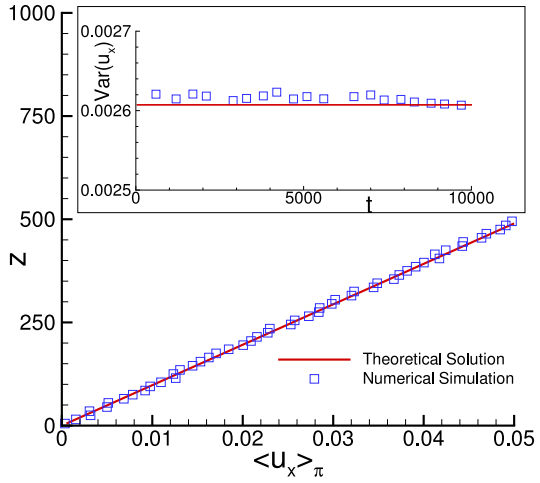

Fig. 2. Main panel: Mean velocity field along the flux direction for the stochastic Couette Flow. Inset: the variance of the velocity fluctuations versus time.

et al., 2012; Donev et al., 2014). and an explicit second-order Runge–Kutta scheme for time advancement, see Gallo et al. (2021), Magaletti et al. (2022) and Gallo et al. (2018a). The spatial discretization ensures exact mass conservation, a crucial ingredient in nucleation studies.

Lennard-Jones units are used throughout the paper. At the temperature $\theta = 1.25$, the metastability density range of an LJ fluid is $\rho_{met} \in (0.439, 0.511)$. Two different thermodynamic conditions are addressed with the initial metastable densities $\rho = 0.47, 0.48$. Following (Gallo et al., 2018b), the dimensionless surface tension is $\sigma = 5.9 \times 10^{-2}$, where $\sigma_{ref} = \epsilon/L_{ref}^2$. The equation of state (LJ fluid) uniquely determines the capillary coefficient to reproduce surface tension value obtained through Monte Carlo simulations, $\lambda = 5.224$, with $\lambda_{ref} = (\sigma^5\epsilon)/m^2$ (Gallo et al., 2018b; Gallo, 2022).

4. Nucleation in flowing liquids

Before nucleation, a statistical steady state is achieved. In Fig. 2 the numerical mean velocity field in $\hat{\mathbf{x}}$ direction ($\langle u_x \rangle_\pi$) is reported as a function of z (blue squares). The mean fields are evaluated as

$$\langle u_x(z)\rangle_\pi = \frac{1}{tA}\int_0^t \mathrm{d}\tau \int_\pi u_x(x,y,z,\tau)\,\mathrm{d}x\mathrm{d}y \tag{4}$$

with A the wall area, and $t = 1000$ non-dimensional times. The continuum red line corresponds to the deterministic Couette solution. The mean velocity profile follows the classical Couette law, $\langle \mathbf{u}(x,y,z)\rangle = U_{wall}\, z/L_z\, \hat{\mathbf{x}}$. In the inset of Fig. 2 the variance of the velocity field in the $\hat{\mathbf{x}}$ direction is reported as a function of time. The blue squares represent the numerical data, and they are evaluated as

$$\mathrm{Var}\left[u_x(t)\right] = \frac{1}{V}\int_V (u_x(x,y,z,t) - \langle u_x(z)\rangle_\pi)^2\,\mathrm{d}x\mathrm{d}y\mathrm{d}z. \tag{5}$$

The numerical value is compared with the theoretical predictions (red lines), with $\mathrm{Var}[u_x] = k_B\theta_0/(\rho_0 \Delta V)$ (Landau and Lifshitz, 1980). θ_0 is the mean temperature of the system, ρ_0 the mean density and ΔV the volume of the numerical cell.

Different snapshots of the nucleation dynamics are reported in Fig. 3 for typical values of liquid density and capillary number. After an initial incubation phase, vapor embryos begin to form, and, once the critical size is exceeded, the bubbles grow in the mother phase. During this stage, the number of supercritical bubbles increases linearly in time. Afterwards, some of them collapse or coalesce, leading to a stationary number of mature vapor bubbles.

In general, bubbles are nucleated both at the wall and in the bulk, though with different relative weights depending on wall wettability and thermodynamic conditions. At the qualitative level, when the activation energy is not high (this case is provided in Fig. 3, top), the difference between the homogeneous and the heterogeneous nucleation barrier is small ($\Delta\Omega_{het} = \Psi(\phi)\Delta\Omega_{hom}$ according to CNT arguments, see below for the definition of the geometric factor Ψ), but the number of nucleation sites available in the bulk is significantly larger than at the walls. As a consequence, many nucleated bubbles are contributed by the bulk. The opposite happens at lower metastability levels (high energy barriers), where the wall overwhelms the bulk and nucleation predominantly takes place at the wall (Fig. 3, bottom).

It is known (Rallison, 1984) that the asphericity $a = (l_M - l_m)/(l_M + l_m)$ of a bubble subject to shear, where l_M and l_m are the bubble major and minor axes ($a = 0/1$ corresponds to a sphere and a long slender bubble, respectively) is proportional to the capillary number, $a = \mathcal{O}(\mathrm{Ca})$. We conclude that the flow does not distort the density profile of the critical nucleus $\rho^*(r)$, also at the largest values of the shear rate we have considered. Hence for the sole purpose of analyzing the evolution of the nucleation process under flow, the critical bubble is identified with that provided by the string method (Gallo et al., 2018b, 2021) in a quiescent fluid. The volume of the critical bubble can be defined as $V_b^* = 4\pi R^{*3}/3$, where $R^* = \int_0^\infty r^3(d\rho/dr)^2dr / \int_0^\infty r^2(d\rho/dr)^2dr$. For nucleation at the wall, the critical volume is obtained by reducing the volume of the bulk critical nucleus by the geometrical factor $\Psi(\phi) = 1/4(1+\cos(\phi))^2(2-\cos(\phi))$, as suggested by CNT.

After defining a bubble as the connected set where $\rho(\boldsymbol{x}) < \rho^*(R^*)$, Fig. 4.a provides the total number of supercritical bubbles (bubble volume larger than critical, $V_b \geq V_b^* = 4\pi R^{*3}/3\Psi(\phi)$) detected in the field for several values of Ca.

Initially, the number of bubbles (both those nucleated in the bulk and at the walls) grows almost linearly. The slope of the linear part (see inset of the figure) provides the nucleation rate, $J_{\mathrm{wall}} = 1/A\dot{N}_{\mathrm{wall}}$ and $J_{\mathrm{bulk}} = 1/A\dot{N}_{\mathrm{bulk}}$ which is defined as the number of supercritical bubbles formed per unit time and area/volume, for heterogeneous/homogeneous nucleation, respectively. In practice, the nucleation rate is found by counting the number of bubbles $N_{\mathrm{wall/bulk}}$ exceeding a certain threshold larger than the critical size. The slope of the $N_{\mathrm{wall/bulk}}$ vs time curves is found to be substantially independent of the adopted threshold consistent with the findings of MD simulations (Diemand et al., 2013; Ayuba et al., 2018). Fig. 4.b depicts the histogram of the critical bubble distribution as a function of the wall-normal coordinate z ($z = 0$ and $z = 500$ represent the wall position). When the fluid metastability is high, bubbles are uniformly detected both in the bulk and on the wall for all the analyzed values of Ca. Conversely, for low metastability bubbles are mainly nucleated on the wall. The homogeneous/heterogeneous nucleation rates normalized with their values in the absence of fluxes $J(0)$, are reported in Fig. 4.c for different Ca. For small values ($\mathrm{Ca} \leq 10^{-2}$), the nucleation rate is not influenced by the hydrodynamic flow, $J/J(0) \simeq 1$. When $\mathrm{Ca} > 10^{-2}$, $J/J(0)$ starts increasing up to 3–4 times the value in the absence of flow.

The relevant difference in the nucleation rate in the presence of macroscopic flows could be ascribed to the role of non-equilibrium effects in nucleation. *Large deviation theory* arguments show that far from equilibrium, critical configurations (instantons) are related to the specific form of the macroscopic velocity fields, meaning that, the classical equilibrium theories are not suitable for quantitatively describing nucleation in non-equilibrium processes (Zakine and Vanden-Eijnden, 2023). This is in line with our results for small values of Ca where the nucleation is not affected by the flows and the process can be interpreted as quasi-static. On the other hand, when the velocity starts increasing non-equilibrium effects emerge. Peculiarly our findings are in line with (Heymann and Vanden-Eijnden, 2008), where the Freidlin–Wentzell theory is used to quantify the most likely nucleation path in the advected Cahn–Hilliard model. This behavior is also observed in crystal nucleation in flowing liquids (Mura and Zaccone, 2016). Fig. 4.d shows the normalized heterogeneous nucleation rate at changing the

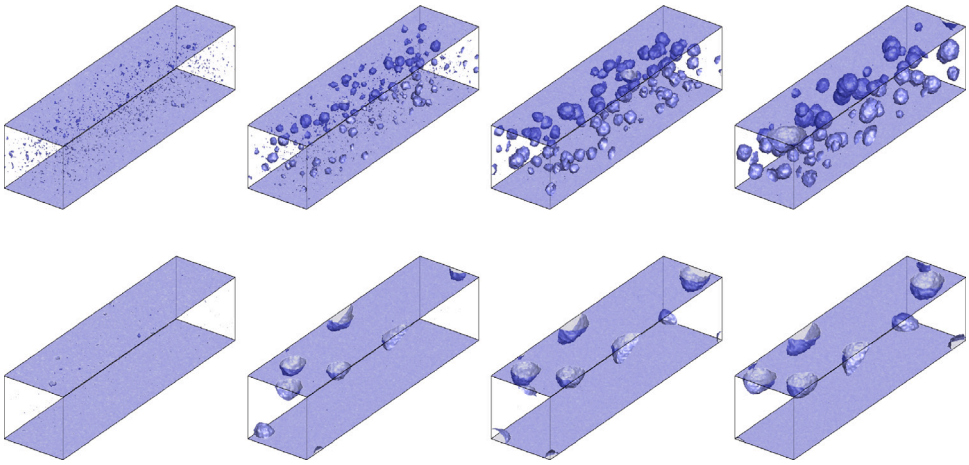

Fig. 3. Snapshots along the bubble nucleation process. Top: $\rho = 0.47$, Ca $= 10^{-2}$ $t = (0.5, 1.5, 3.0\ 6.0) \times 10^4$; $\rho = 0.47$, Ca $= 10^{-2}$. Bottom: $\rho = 0.48$, Ca $= 1.0 \times 10^{-2}$ $t = (3.0, 6.0, 9.0, 1.2) \times 10^5$; In both cases, the system volume is $V = 500 \times 500 \times 2000$.

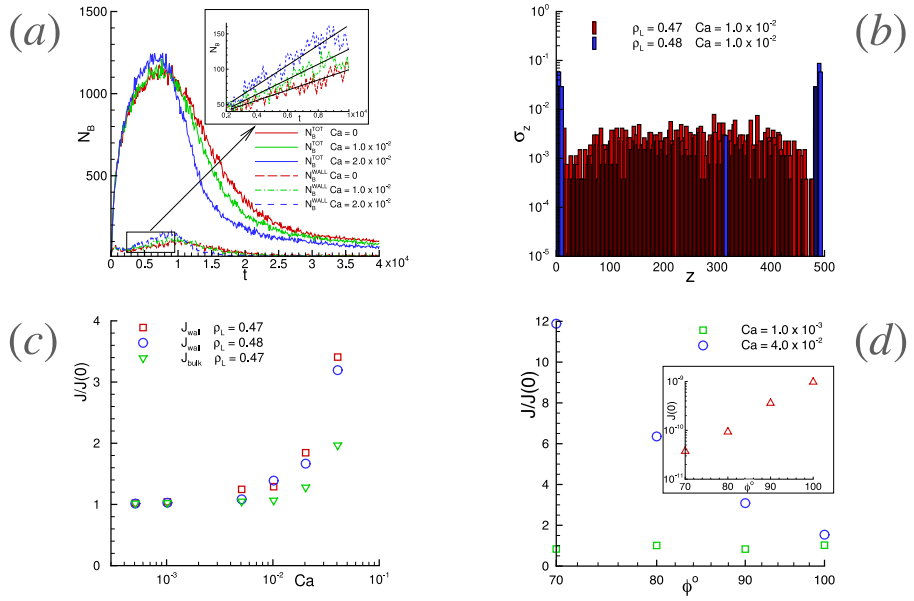

Fig. 4. Panel (a): Number of supercritical bubbles detected in the field in time. The initial metastable liquid density is $\rho = 0.47$. Solid lines refer to the bulk bubbles and dashed ones to the bubble detected on the wall. In the inset, a zoom on the linear part of the curves (where the nucleation rate is measured) is reported. Panel (b): Istogram of bubble distribution in z direction. Two different values of Ca and initial densities are reported. Panel (c): Homogeneous and heterogeneous Nucleation rates normalized with $J(0)$, which corresponds to the nucleation rate in the absence of flow. Panel (d): Heterogeneous nucleation rate as a function of a contact angle ϕ. The initial liquid density is $\rho = 0.48$ and two different values of Ca. In the inset is reported the nucleation rate $J(0)$ as a function of the contact angle ϕ.

wall wettability with $J(0)$, reported as a function of the contact angle ϕ in the inset,consistent with the CNT prediction (Blander and Katz, 1975). In fact, the energy barrier depends on the wall wettability and increases (decreases) for hydrophilic (hydrophobic) chemistry. In addition, we evaluate the influence of the hydrodynamic flow on the scaling of the rate with the contact angle. For small Ca (Ca $= 1.0 \times 10^{-3}$), the flow does not affect the rate scaling ($J/J(0) = $ const). However when Ca increases (Ca $= 4.0 \times 10^{-2}$), $J/J(0)$ becomes a decreasing function of ϕ.

Let us focus now on the nucleation stage, where after the incubation time t^*, the number of bubbles increases linearly in time, $N(t) = \bar{n} V t\, \Theta(t - t^*)$, where $\Theta(t - t^*)$ is the Heaviside step function and $\bar{n}$ is the mean bubble number density. In the linear stage $J = \bar{n}$. Similar arguments apply to the rate per unit area when dealing with heterogeneous nucleation. MD simulations as well as theoretical approaches only have access to the nucleation rate, preventing the study of the spatial distribution of nucleation embryos. The main limitation of atomistic simulations concerns the dimension of the simulated system, which is often too small to have statistically robust information about the spatial distribution of the nuclei. On the other hand, theoretical approaches deal with mean first passage time and nucleation rate. Here, to measure these important quantities, large-scale vapor bubble nucleation simulations are performed. In particular, a system volume of $V = 3000^3$ (that is $V \simeq 1\ \mu\text{m}^3$) is employed at $\rho = 0.47$ to determine the homogeneous spatial distribution of the nucleation sites. Concerning heterogeneous simulations, numerical experiments with extended walls $A = 10000^2$ are conducted in the same thermodynamic conditions. In both cases, up to 30,000 vapor bubble nucleation events are detected and a Voronoi tessellation is employed to infer spatial distribution statistics. Panel (a) of Fig. 5 reports a Voronoi diagram during heterogeneous nucleation at the wall, the bubbles are identified with their center of mass (red points), and the analysis is conducted during the nucleation phase ($t > t^*$). The measure of the Voronoi cell (area in heterogeneous conditions and volume for the homogeneous one) gives access to the mean bubble number density value at time t. For instance, the mean value of the

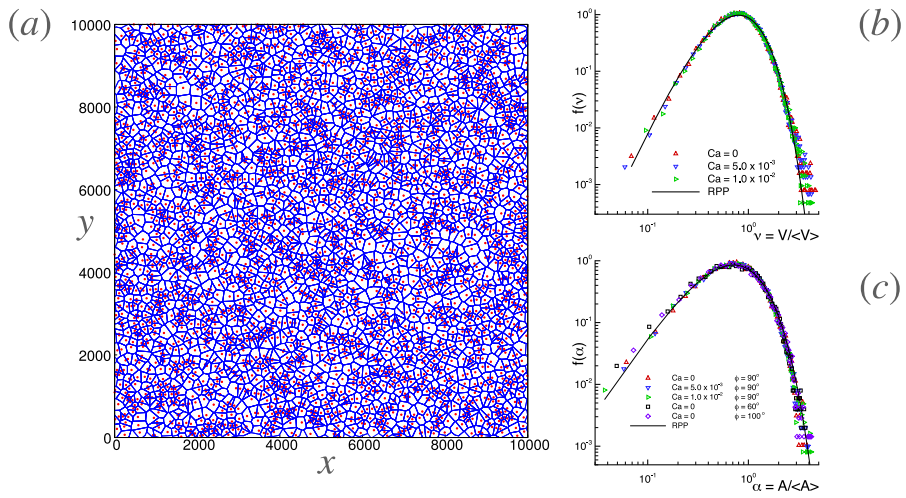

Fig. 5. Panel (a): Two-dimensional Voronoi Tessellation of supercritical bubbles detected on the wall. Panel (b): Pdf of normalized Voronoi cell volumes (homogeneous nucleation) for different values of Ca. Panel (c): Pdf of the normalized measure of Voronoi cell areas (heterogeneous nucleation), different values of Ca and hydrophilic and hydrophobic cases are reported. In both cases, the comparison with a Random Poisson Process (RPP) is reported as a black solid line.

Voronoi cell volume is $\langle V_i \rangle = V/N(t) = (\bar{n}t)^{-1}$, leading to

$$J = -\frac{1}{\langle V_i \rangle^2} \frac{\mathrm{d}\langle V_i \rangle}{\mathrm{d}t}. \tag{6}$$

Replacing the cell volume with the wall cell area, the above equation holds also for the heterogeneous case. Furthermore, the probability distribution function of the normalized Voronoi cell measure. e.g. $\alpha = A_i/\langle A_i \rangle$ for heterogeneous nucleation and $\nu = V_i/\langle V_i \rangle$ provides information about preferential concentrations, e.g. voids and clustering. In Fig. 5 panels (b,c) we report the pdfs of the normalized cell size ν (panel (b)) and α (panel (c)) for different Ca and different wall wettabilities. The comparison with a Poisson Random Process (RPP) is also shown. The RPP pdf depends on the dimensionality of the Voronoi tessellation and is reported in Ferenc and Néda (2007). In our case we adopted $f(\alpha) = 343/15\sqrt{7/2\pi}\alpha^{5/2}\exp(-7/2\alpha)$ and $f(\nu) = 3125/24\nu^4\exp(-5\nu)$. The agreement with the RPP is very good both in homogeneous and heterogeneous conditions for all the simulations we have analyzed. However, the data seem to suggest a slight trend to clustering, where the probability of finding a small Voronoi cell a little higher than an RPP is detected in both panels of Fig. 5. At large scales, the hydrodynamic expansion of the firstborn bubbles makes the probability of observing bigger Voronoi cells higher for the homogeneous case. This effect is not observed at the wall (heterogeneous nucleation, panel c). Overall, numerical data support the interpretation of the nucleation process as an RPP according to which the number of bubbles falling in a domain $\mathcal{V}$, with measure V, at time t, $N_{\mathcal{V}}(t) = \sum_k \mathbf{1}_{(\mathbf{x}_k \in \mathcal{V})}$, with $\mathbf{1}$ the set indicator function, is distributed according to the PDF

$$P\left(N_{\mathcal{V}}(t) = m\right) = \exp\left(-\Lambda_t V\right)\frac{\left(\Lambda_t V\right)^m}{m!}, \tag{7}$$

where Λ_t is the time-dependent RPP intensity. After the supercritical bubbles start forming (see Fig. 4 panel (a)), their number grows linearly in time, i.e. $\Lambda_t \simeq \dot{\Lambda}_0 t$, thus the mean value of nucleated bubble is $\langle N(t) \rangle = \dot{\Lambda}_0 V t$. By comparing the Poisson expected value of $N(t)$ with the nucleation rate definition, one has $J = \dot{\Lambda}_0$, leading to

$$P\left(N(t) = m\right) = \exp\left(-JtV\right)\frac{(JtV)^m}{m!}. \tag{8}$$

5. Conclusions

In this work, we have numerically addressed the problem of vapor nucleation in flowing liquids. The physical problem is relevant both from a fundamental and applicative point of view. In fact, the intrinsic non-equilibrium nature of hydrodynamic flows makes the description of the thermally activated process very challenging, ruling out, in principle, the use of equilibrium results (Grafke et al., 2015; Grafke and Vanden-Eijnden, 2019). *In silico* experiments based on fluctuating hydrodynamics naturally extend into the non-equilibrium regime and can be seen as a valuable instrument to address phase change in flowing fluids, giving access to the main nucleation observables in macroscopic flows. For all the analyzed fluid configurations, the nucleation process can be modeled as a stochastic RPP process fully characterized by the nucleation rate. Most often, Ca $\leq 10^{-2}$ and the nucleation rate is substantially unaffected by the shear rate. For pure liquids, given the small size of the nuclei, this is the usual case unless the shear is extremely large or dissolved gases increase the size of the nuclei. In these conditions, a significant dependency of the nucleation rate on the shear rate is observed, with J raising four times larger in applications like bearings of cryogenic turbo pumps.

The results we have found can be used to build multiscale approaches from nucleation to macroscopic hydrodynamics (millimeter-sized bubbles). The proposed multiscale approach describes the liquid–vapor phase change process from nanoscale nucleation to the nucleated phase's hydrodynamics (growth and transport) at the micron scale. Deciphering the stochastic fluid mechanics of this mesoscale region is particularly crucial, as it is too extensive for molecular dynamics simulations and yet not addressable by traditional multiphase hydrodynamics. This intermediate scale, where nucleation starts and develops, is the missing link between atomistic and continuum theories of phase change. For flowing liquids, as far as the shear rate is not too high, improvements in nucleation modeling in quiescent fluids (Menzl et al., 2016; Magaletti et al., 2021) provide a precise estimation of the nucleation rate and can be complemented with the stochastic RPP description to generate an input bubble population for macroscopic analysis. When the capillary number is larger, the same approach can be used, provided the nucleation rate is extracted from dedicated mesoscale simulations like those presented here.

CRediT authorship contribution statement

M. Gallo: Writing – review & editing, Writing – original draft, Software, Methodology, Investigation, Formal analysis, Data curation, Conceptualization. **C.M. Casciola:** Writing – review & editing, Investigation, Funding acquisition, Formal analysis, Conceptualization.

Declaration of competing interest

The authors declare that they have no known competing financial interests or personal relationships that could have appeared to influence the work reported in this paper.

Data availability

Data will be made available on request.

Acknowledgments

This work has been supported by Italian PNRR funds, Italy, CN-1 Spoke 6. Support is acknowledged by the CINECA award under the ISCRA initiative, for the availability of high-performance computing resources and support (ISCRA-B D-RESIN). C.M.C. has been partially supported by the Sapienza 2022 Funding Scheme, Project No. RG1221815884CB65. C.M.C. and M.G. have received financial support from ICSC – Centro Nazionale di Ricerca in "High-Performance Computing, Big Data and Quantum Computing", funded by the European Union – NextGenerationEU.

References

Abbondanza, D., Gallo, M., Casciola, C.M., 2022. Cavitation over solid surfaces: Microbubble collapse, shock waves, and elastic response. Meccanica 1–11.

Abbondanza, D., Gallo, M., Casciola, C.M., 2023. Diffuse interface modeling of laser-induced nano-/micro-cavitation bubbles. Phys. Fluids 35 (2).

Ayuba, S., Suh, D., Nomura, K., Ebisuzaki, T., Yasuoka, K., 2018. Kinetic analysis of homogeneous droplet nucleation using large-scale molecular dynamics simulations. J. Chem. Phys. 149 (4), 044504.

Balboa, F., Bell, J.B., Delgado-Buscalioni, R., Donev, A., Fai, T.G., Griffith, B.E., Peskin, C.S., 2012. Staggered schemes for fluctuating hydrodynamics. Multiscale Model. Simul. 10 (4), 1369–1408.

Blander, M., Katz, J.L., 1975. Bubble nucleation in liquids. AIChE J. 21 (5), 833–848.

Bottacchiari, M., Gallo, M., Bussoletti, M., Casciola, C.M., 2022. Activation energy and force fields during topological transitions of fluid lipid vesicles. Commun. Phys. 5 (1), 1–12.

Bottacchiari, M., Gallo, M., Bussoletti, M., Casciola, C.M., 2024. The local variation of the gaussian modulus enables different pathways for fluid lipid vesicle fusion. Sci. Rep. 14 (1), 23.

Brennen, C.E., 2015. Cavitation in medicine. Interface Focus 5 (5), 20150022.

Brentnall, M.D., Martin, R.W., Vaezy, S., Kaczkowski, P., Forster, F., Crum, L., 2001. A new high intensity focused ultrasound applicator for surgical applications. IEEE Trans. Ultrason. Ferroelectr. Freq. Control 48 (1), 53–63.

Chakraborty, B., Gallo, M., Marengo, M., De Coninck, J., Casciola, C.M., Miche, N., Georgoulas, A., 2024. Multi-scale modelling of boiling heat transfer: Exploring the applicability of an enhanced volume of fluid method in sub-micron scales. Int. J. Thermofluids 22, 100683.

Chaudhri, A., Bell, J.B., Garcia, A.L., Donev, A., 2014. Modeling multiphase flow using fluctuating hydrodynamics. Phys. Rev. E 90 (3), 033014.

Chen, B., Siepmann, J.I., Klein, M.L., 2005. Simulating vapor- liquid nucleation of water: A combined histogram-reweighting and aggregation-volume-bias Monte Carlo investigation for fixed-charge and polarizable models. J. Phys. Chem. A 109 (6), 1137–1145.

Chen, B., Siepmann, J.I., Oh, K.J., Klein, M.L., 2001. Aggregation-volume-bias Monte Carlo simulations of vapor–liquid nucleation barriers for lennard-jonesium. J. Chem. Phys. 115 (23), 10903–10913.

Debenedetti, P.G., 1996. Metastable Liquids: Concepts and Principles. Princeton University Press.

Diemand, J., Angélil, R., Tanaka, K.K., Tanaka, H., 2013. Large scale molecular dynamics simulations of homogeneous nucleation. J. Chem. Phys. 139 (7), 074309.

Donev, A., Nonaka, A., Sun, Y., Fai, T., Garcia, A., Bell, J., 2014. Low mach number fluctuating hydrodynamics of diffusively mixing fluids. Commun. Appl. Math. Comput. Sci. 9 (1), 47–105.

Durán-Olivencia, M.A., Yatsyshin, P., Goddard, B.D., Kalliadasis, S., 2017. General framework for fluctuating dynamic density functional theory. New J. Phys. 19 (12), 123022.

Ferenc, J.-S., Néda, Z., 2007. On the size distribution of Poisson Voronoi cells. Phys. A 385 (2), 518–526.

Gallo, M., 2022. Thermal fluctuations in metastable fluids. Phys. Fluids 34 (12), 122011.

Gallo, M., Magaletti, F., Casciola, C.M., 2018a. Fluctuating hydrodynamics as a tool to investigate nucleation of cavitation bubbles. In: Multiphase Flow: Theory and Applications. p. 347.

Gallo, M., Magaletti, F., Casciola, C.M., 2018b. Thermally activated vapor bubble nucleation: The Landau-Lifshitz–van der Waals approach. Phys. Rev. Fluids 3, 053604. http://dx.doi.org/10.1103/PhysRevFluids.3.053604, URL https://link.aps.org/doi/10.1103/PhysRevFluids.3.053604.

Gallo, M., Magaletti, F., Casciola, C.M., 2021. Heterogeneous bubble nucleation dynamics. J. Fluid Mech. 906.

Gallo, M., Magaletti, F., Cocco, D., Casciola, C.M., 2020. Nucleation and growth dynamics of vapour bubbles. J. Fluid Mech. 883.

Gallo, M., Magaletti, F., Georgoulas, A., Marengo, M., De Coninck, J., Casciola, C.M., 2023. A nanoscale view of the origin of boiling and its dynamics. Nature Commun. 14 (1), 6428.

Goddard, B.D., Nold, A., Savva, N., Pavliotis, G.A., Kalliadasis, S., 2012. General dynamical density functional theory for classical fluids. Phys. Rev. Lett. 109 (12), 120603.

Grafke, T., Grauer, R., Schäfer, T., 2015. The instanton method and its numerical implementation in fluid mechanics. J. Phys. A 48 (33), 333001.

Grafke, T., Vanden-Eijnden, E., 2019. Numerical computation of rare events via large deviation theory. Chaos 29 (6).

Heymann, M., Vanden-Eijnden, E., 2008. Pathways of maximum likelihood for rare events in nonequilibrium systems: application to nucleation in the presence of shear. Phys. Rev. Lett. 100 (14), 140601.

Johnson, J.K., Zollweg, J.A., Gubbins, K.E., 1993. The Lennard-Jones equation of state revisited. Mol. Phys. 78 (3), 591–618.

Kathmann, S.M., Schenter, G.K., Garrett, B.C., Chen, B., Siepmann, J.I., 2009. Thermodynamics and kinetics of nanoclusters controlling gas-to-particle nucleation. J. Phys. Chem. C 113 (24), 10354–10370.

Landau, L., Lifshitz, E., 1980. Statistical Physics, Vol. 5. In: Course of theoretical physics, vol. 30.

Lutsko, J.F., 2012. A dynamical theory of nucleation for colloids and macromolecules. J. Chem. Phys. 136 (3), 034509.

Lutsko, J.F., 2019. How crystals form: A theory of nucleation pathways. Sci. Adv. 5 (4), eaav7399.

Maeda, K., Maxwell, A.D., Colonius, T., Kreider, W., Bailey, M.R., 2018. Energy shielding by cavitation bubble clouds in burst wave lithotripsy. J. Acoust. Soc. Am. 144 (5), 2952–2961.

Magaletti, F., Gallo, M., Casciola, C.M., 2021. Water cavitation from ambient to high temperatures. Sci. Rep. 11 (1), 1–10.

Magaletti, F., Gallo, M., Marino, L., Casciola, C.M., 2016. Shock-induced collapse of a vapor nanobubble near solid boundaries. Int. J. Multiph. Flow 84, 34–45.

Magaletti, F., Gallo, M., Perez, S.P., Carrillo, J.A., Kalliadasis, S., 2022. A positivity-preserving scheme for fluctuating hydrodynamics. J. Comput. Phys. 463, 111248.

Menzl, G., Gonzalez, M.A., Geiger, P., Caupin, F., Abascal, J.L., Valeriani, C., Dellago, C., 2016. Molecular mechanism for cavitation in water under tension. Proc. Natl. Acad. Sci. 113 (48), 13582–13587.

Miller, D.L., Song, J., 2003. Tumor growth reduction and DNA transfer by cavitation-enhanced high-intensity focused ultrasound in vivo. Ultrasound Med. Biol. 29 (6), 887–893.

Municchi, F., Markides, C., Matar, O., Magnini, M., 2024. Computational study of bubble, thin-film dynamics and heat transfer during flow boiling in non-circular microchannels. Appl. Therm. Eng. 238, 122039.

Mura, F., Zaccone, A., 2016. Effects of shear flow on phase nucleation and crystallization. Phys. Rev. E 93 (4), 042803.

Ohl, C.-D., Arora, M., Dijkink, R., Janve, V., Lohse, D., 2006. Surface cleaning from laser-induced cavitation bubbles. Appl. Phys. Lett. 89 (7), 074102.

Qiu, M., Chen, L., Li, Y., Yan, J., 2017. Sliding bearing lubrication theory. In: Bearing Tribology. Springer, pp. 101–143.

Rallison, J., 1984. The deformation of small viscous drops and bubbles in shear flows. Annu. Rev. Fluid Mech. 16 (1), 45–66.

Silvani, G., Scognamiglio, C., Caprini, D., Marino, L., Chinappi, M., Sinibaldi, G., Peruzzi, G., Kiani, M.F., Casciola, C.M., 2019. Reversible cavitation-induced junctional opening in an artificial endothelial layer. Small 15 (51), 1905375.

Steinkühler, J., Knorr, R.L., Zhao, Z., Bhatia, T., Bartelt, S.M., Wegner, S., Dimova, R., Lipowsky, R., 2020. Controlled division of cell-sized vesicles by low densities of membrane-bound proteins. Nat. Commun. 11 (1), 1–11.

Tomita, Y., Shima, A., 1986. Mechanisms of impulsive pressure generation and damage pit formation by bubble collapse. J. Fluid Mech. 169, 535–564.

Zakine, R., Vanden-Eijnden, E., 2023. Minimum-action method for nonequilibrium phase transitions. Phys. Rev. X 13 (4), 041044.

Zhang, L., Gong, S., Lu, Z., Cheng, P., Wang, E.N., 2022. Boiling crisis due to bubble interactions. Int. J. Heat Mass Transfer 182, 121904.

Zhang, Y., Guo, Z., Gao, Y., Du, X., 2018. Acoustic wave propagation in bubbly flow with gas, vapor or their mixtures. Ultrason. Sonochem. 40, 40–45.

Zhang, L., Wang, C., Su, G., Kossolapov, A., Matana Aguiar, G., Seong, J.H., Chavagnat, F., Phillips, B., Rahman, M.M., Bucci, M., 2023. A unifying criterion of the boiling crisis. Nature Commun. 14 (1), 2321.